Ground Penetrating Radar for Belowground Phenotyping of High-biomass Grasses for Soil Carbon Sequestration

Matthew Wolfe (mwolfe45@gmail.com)
Texas A&M University https://orcid.org/0000-0002-8076-1509
Da Huo
Texas A&M University
Henry Ruiz-Guzman
Texas A&M University
Brody Teare
Texas A&M University
Tyler Adams
Texas A&M University
Iliyana Dobreva
Texas A&M University
Mark Everett
Texas A&M University
Michael Bishop
Texas A&M University
Russell Jessup
Texas A&M University
Dirk Hays
Texas A&M University

Research Article

Keywords: Climate change, Carbon sequestration, Root phenotyping

Posted Date: December 1st, 2021

DOI: https://doi.org/10.21203/rs.3.rs-1041672/v1

Abstract

Aims

Many governments and companies have committed to moving to net-zero emissions by 2030 or 2050 to tackle climate change, which require the development of new carbon capture and sequestration/storage (CCS) techniques. A proposed method of sequestration is to deposit carbon in soils as plant matter including root mass and root exudates. Adding perennial traits such as rhizomes to crops as part of a sequestration strategy would result in annual crop regrowth from rhizome meristems rather than requiring replanting from seeds which would in turn encourage no-till agricultural practices. Integrating these traits into productive agriculture requires a belowground phenotyping method compatible with high throughput breeding and selection methods (i.e., is rapid, inexpensive, reliable, and non-invasive), however none currently exist.

Methods

Ground penetrating radar (GPR) is a non-invasive subsurface sensing technology that shows potential as a phenotyping technique. In this study, a prototype GPR antenna array was used to scan roots of the perennial sorghum hybrid, PSH09TX15. A-scan level time-domain analyses and B-scan level time/frequency analyses using the continuous wavelet transform were utilized to extract features of interest from the acquired radargrams.

Results

Of six A-scan diagnostic indices examined, the standard deviation of signal amplitude correlated most significantly with belowground biomass. Time frequency analysis using the continuous wavelet transform yielded high correlations of B-scan features with belowground biomass.

Conclusion

These results demonstrate that continued refinement of GPR data analysis workflows should yield a highly applicable phenotyping tool for breeding efforts in environments where selection is otherwise impractical on a large scale.

1. Introduction

Ongoing climate change due to global temperature increase affects all Earth systems. Global average temperature has increased by 0.85°C between 1880 and 2012, and is expected to reach 1.5°C above preindustrial temperatures by 2040 (Allen, M.R., O.P. Dube, W. Solecki, F. Aragón-Durand, W. Cramer, S. Humphreys, M. Kainuma, J. Kala, N. Mahowald, Y. Mulugetta, R. Perez, M. Wairiu 2018). Human activity has helped drive atmospheric concentrations of carbon dioxide, methane, and nitrous oxide species to unprecedented levels in the Holocene geological epoch. Among these, CO_2 is responsible for 20% of thermal energy absorbed by Earth's atmosphere (Schmidt et al. 2010). The increase in atmospheric

carbon and resulting warming due to the greenhouse effect has severe negative ramifications for many important ecological systems on a planet-wide scale. The Great Barrier Reef, for example, has sustained irreparable damage in recent years (Kerry et al. 2017). A recent study of the variance in maximum temperature tolerance among insect species demonstrates that at current rates of warming, a substantial number of species will be at risk of extinction within the next century (García-robledo et al. 2016). The rise in global average temperatures brings with it a higher incidence of extreme weather events (2016). Political and humanitarian ramifications as a result of these events are already being noticed: in 2008 the flooding of the Zambezi River in Mozambique resulted in the displacement of 80,000 people; while in North America, extreme weather including record-setting heat waves has resulted in an increase in death rates and health problems (Allen, M.R., O.P. Dube, W. Solecki, F. Aragón-Durand, W. Cramer, S. Humphreys, M. Kainuma, J. Kala, N. Mahowald, Y. Mulugetta, R. Perez, M. Wairiu 2018).

A viable strategy to achieve net-negative emissions is the recapture and storage of atmospheric carbon as recalcitrant plant mass. A variety of plant materials have been proposed for this task. Among these, grass species have been suggested as efficient targets of sequestration efforts through restoration and establishment of natural grasslands or improvement of the carbon sequestration potential of dominant cereal crops. Grasslands can sequester up to ~3 Mg of C per hectare per year (Resource and Collins 2001). Grasses also serve as a carbon sink in agricultural settings. Lemus *et al.* estimated that ~750 Mha are available globally for conversion to bioenergy cultivation, with an estimated sequestration potential of ~1600 Tg C y-1 (Lemus and Lal 2005). Bioenergy cultivation provides an additional benefit of producing a carbon-neutral source of energy, as above-ground material could be harvested and utilized without releasing additional greenhouse gasses (Lemus and Lal 2005). In addition, addition of perenniality conferring traits such as rhizomes to current grain crops such was wheat, rice, barley, maize, sorghum and millets could increase their carbon sequestration potential several-fold on the 730 Mha on which they are produced compared to current fibrous root cereals. Moreover, establishment of perennial grain and bioenergy crops raises the prospect of a semi-permanent root and rhizome system which would continuously deposit carbon in the form of living rhizomes, their attached fibrous roots and senesced crown derived fibrous root, root exudate, and senesced root hairs. Perenniality, the ability for a plant to regrow after a single growing season, is a term that is given to the collective action of several interacting plant traits. Thomas *et al.* (Thomas et al. 2000) describes perenniality as the retention of an indeterminate apical meristem beyond one growing season. Continuous presence of perennial grasses in an agricultural field makes these grasses ideal for conservation tillage, and their continuous or seasonal photosynthetic activity results in year-round conversion of atmospheric CO_2 to plant biomass (Ledo et al. 2020).

The results of a core-based soil sampling study comparing cropland, native pastures, and land managed under the Conservation Reserve Program reported by Gebhart *et al.* (1994) estimates that increases of 0.8 metric tons C ha^{-1} yr^{-1} to a depth of 40 cm, and 1.1 metric tons C ha^{-1} yr^{-1} to a depth of 300 cm were possible using grass species (Gebhart et al. 1994). Optimizing the system with respect to belowground deposition would potentially lead to a viable climate change mitigation technique. A step toward such an

optimization is the systematic study and refinement of root and rhizome traits in particular through breeding efforts. The scale required by breeding strategies requires a fast and efficient means of phenotyping root traits; however there is currently no method that meets these requirements. Maximizing belowground biomass necessarily relies on high-throughput phenotyping methods for making trait selections in field trials. Current methods of root phenotyping in a field setting provide high quality root information, however some aspects of these methods are unattractive for plant breeders: they tend to be labor intensive, challenging due to inherent field variability, require a secondary cleaning of root samples, and are destructive (Paez-Garcia et al. 2015). Recent studies have shown that increasing the quantity of the acquired phenotypic data collected can overcome an increased error rate, making high-throughput phenotyping an attractive alternative to manual phenotyping methods (Lane and Murray 2021). Ground penetrating radar (GPR) is emerging as a potential high-throughput and non-destructive root phenotyping technique and its principles are discussed below.

GPR is a geophysical technique that uses electromagnetic waves in the MHz-GHz frequency range to image subsurface structure. The technique operates by first sending a pulse of energy into the ground and then recording the resulting time-variations in the returned field amplitude caused by scattering, reflection, and diffraction of the pulse due to subsurface discontinuities in electromagnetic wave impedance. Tree roots were among the first botanical targets studied. Given their large diameter, they are readily detected by GPR. As such, the majority of early root studies using GPR are within the field of forestry. Beyond simple detection, studies by Butnor et. al (Butnor et al. 2001) (Butnor et al. 2003) indicate the possibility of predicting tree root biomass based on GPR signals. Theoretically, the technology should also be able to detect the roots of agronomic crops, and as such GPR is attracting research interest in agriculture. GPR was recently applied to the detection of peanuts growing in a field setting (Dobreva et al. 2021). The antenna used in that study operates over the frequency range 0.9 GHz to 2.7 GHz. A λ/4 rule of thumb, where λ is the electromagnetic wavelength in the subsurface medium, is applicable be used to determine the smallest separation necessary to distinguish between two nearby objects (Everett 2013). The minimum separation, or so-called "detection threshold", varies depending on the velocity of the signal in the medium, and in an agricultural context it is largely determined by field moisture levels. Using a range of values of the dielectric constant expected in agricultural soils (typically between 2 and 10), velocities of 0.21 m/ns to 0.09 m/ns, respectively, can be calculated using the equation:

Equation 1:

$$v = \frac{c}{\sqrt{\varepsilon_r}}$$

where c is the speed of light in a vacuum and ε_r is the relative dielectric permittivity, or dielectric constant, of the soil medium (Utsi 2017). In practice, this means that the lowest frequency of the prototype antenna (0.9 GHz) used in this study corresponds to a detection threshold that ranges from 5.89 cm to 2.63 cm, while the highest frequency (2.7 GHz) corresponds to a detection threshold that ranges between 1.96 cm and 0.88 cm. As mentioned above, the image displayed in GPR scans represent reflection, diffraction, and backscatter of electromagnetic energy from objects buried in the subsurface. Visual representations of

the received voltage fluctuations are typically viewed in one of two forms: a single return is displayed as a quasi-oscillatory time-varying function with amplitude peaks and valleys on one axis and time on the orthogonal axis, and is referred to as an 'A-scan'. When a series of A-scans is acquired along a survey path, a pseudo-2D cross section (B-scan) of the subsurface is produced. In such a 2D radargram, the signal amplitude is often represented by brightness on a gray-scale, time is given on the vertical axis, and survey position is given on the horizontal axis.

In this study, the roots of the *Sorghum bicolor* L. Moench x *Sorghum halepense* L. Pers cross PSH09TX15 were scanned *in-situ* using a prototype GPR antenna array (Jessup et al. 2017). The hybrid resulting from the above cross is generally sterile, grows to a height of ~2 m, produces rhizomes with a diameter of ~1 cm from which emanates the fibrous root system (Jessup et al. 2017). This hybrid is of particular interest due to its method of propagation via rhizomes. The latter comprise modified stem tissue that grows laterally beneath the soil surface and produce new clone shoots from their nodes. Rhizomes can persist from season to season, and have been shown to accumulate mass over multiple growing seasons (Xiong and Thomas 2010). Additionally, rhizomes have the capability of growing with a smaller energy investment in each subsequent growing season. This capability results in a crop that can sequester carbon much more effectively than an annual crop.

The objective of this study is to evaluate the capability of GPR to characterize a high-biomass fibrous root system and rhizome system in a controlled environment. Similar studies demonstrating the radar detection of root systems have been performed in species such as cassava, *Manihot esculenta* L. Crantz, and peanut (Dobreva et al. 2021)(Delgado et al. 2017). However, no such studies to date have involved grass species that are suited for carbon sequestration efforts (Delgado et al. 2017). The working hypothesis of this study is that under controlled environmental conditions, grass root systems with high mass deposits are detectable via GPR time-series and time-frequency analyses. To test the hypothesis, the aforementioned sorghum hybrids selected for high belowground biomass were grown as a monoculture in a pure sand environment. The root system was scanned using the prototype GPR antenna, and then harvest biomass information was regressed against features extracted from the radargrams. The features were derived using time-domain analysis on individual A-scans as well as time-frequency analysis on B-scans, the latter analysis being based on the continuous wavelet transform.

2. Material And Methods

2.1 Study site

Plots were characterized by a variable planting density of *S. bicolor* X *S. halepense*. The plants were grown from rhizome propagules for 1 year prior to harvest in a subtropical environment with an average annual rainfall of 101.6 cm. Actual rainfall for the year of growth was ~134.6 cm. Plants were grown in a constructed trough of post and rope support structure to enclose the growth matrix lined within a weed cloth barrier. The trough was filled with 100% silica sand. The facility was constructed aboveground on the Texas A&M University Farm (30.530, -96.426) and is shown in Figure 1. The artificial environment

pictured, referred herein as a 'trough', was divided into 8 plots whose boundaries are defined by the posts making up the wall. Plots were of a variable size, but were on average of length of 2.6 m, width 2.1 m, and depth 1.1 m. Prior to filling the troughs with the sand, nylon nets were installed at three different depths. The nets were used during harvest to separate belowground biomass into different depth zones following a rinsing process. Photographs of the trough setup is shown in Figure 2. Plants were irrigated via a drip tape, and fertigated as needed via liquid fertilizer injector.

Fig 1 Plots and depth levels in the trough environment. From left to right, plots are numbered 1 – 8 (see top view). The space labeled 'B' was designated as a blank area and no associated mass was harvested. The different depth zones are demarcated with different shades of gray

Fig 2 Image of artificial trough environment. **(left)** Belowground biomass following trough washing process. Pictured are the three depth layers separated by the green nylon netting. **(right)**. Artificial trough environment during growing season

2.2 Field Data collection

In October 2017, the aboveground planted PSH09TX1 material was mowed to the soil media surface and the troughs scanned with a prototype air-launched GPR antenna array developed by IDS Georadar (Golden, Colorado). The latter utilizes a unique air-launched resistively loaded-vee dipole antenna design which had been developed as a means to detect buried objects without the necessity of ground contact (Kim and Scott 2005)(Nuzzo et al. 2014)(Montoya and Smith 1996). The antenna array unit has been used in other published research (Dobreva et al. 2021)(Shen et al. 2019).

After the GPR scanning, the weed cloth barrier supporting the sides of the berm (shown in Figure 2, right) was removed exposing the bare sand matrix. The troughs were washed with a high-pressure water hose over the course of one week resulting in the gradual exposure of root material (see Figure 2, left). The fibrous root systems and rhizomes were captured by the nylon nets in the three different accessible depth zones. Measured from the soil surface, the thicknesses of each of the depth zones were 15, 45, and 45 cm (see side view in Figure 1). The fibrous roots and rhizomes were then harvested by hand. Plant crowns were included in the collected tissue of the top zone. Roots were severed where they crossed a nylon nets that separating adjacent depth zones. Roots were collected within each plot (see Figure 1, top) at each of the three depth zones. Harvesting took place immediately after the washing process had concluded, and the root material was dried in a greenhouse in order to preserve labile mass against microbial degradation. The root samples were then re-washed in large plastic containers to remove excess sand. Samples were then hand-separated into two main tissue sub-groups: rhizomatous and fibrous root biomass. Each sample was then dried in an oven at 60°C until its weight stabilized to remove variability in measured mass due to water content.

2.3 GPR processing

The GPR workflow (Figure 3) comprises a small number of key steps. The processing and analysis was performed using GPR-Studio version 1.0.1 (Crop Phenomics LLC, College Station, TX, USA, (cropphenomics.com) (Crop Phenomics)), which is a software combination of graphical user interface and Python library that provides GPR processing, analysis, and visualization services. While performing the exploratory analysis of B-scans, it was found that GPR processing workflows which involved certain widely applied signal processing techniques (bandpass filters, dewow, gain correction) produced inconsistent results. With regards to bandpass filters, at this stage in this field, it is uncertain which frequency ranges correspond to noise and which ranges indicate the presence of target biomass. From Cassidy 2009 (Cassidy 2009): “In general, it is always best to go with the simplest processing options first and stop when there is nothing else to gain from the process.” The net result of any filtering operation is always the removal or at least the alteration of potentially informative features. With this in mind, the final preprocessing workflow is a minimal pipeline, except that dewow was used to compensate for noised from prototype GPR array instrument.

Fig 3 Processing flowcharts. Chart **a)** shows the processing steps used to prepare GPR data for the A-scan analysis and half of the CWT analysis. Chart **b)** shows the processing steps used to prepare GPR data for the second half of the CWT analysis

The initial GPR processing step is the cropping of the B-scan to remove regions known to contain unwanted non-informative signals. The raw B-scan is cropped to exclude the direct wave and associated ground clutter (normally indicated by the high-amplitude bands at the top of the section) as well as any samples recorded after 18 ns two-way travel time (see Figure 4). The latter region appears to contain mostly deeper soil horizons beneath the trough system and/or multiple reflections of shallower structure. Multiples may be generated as a direct result of the engineering of the prototype antenna hardware (verbal comm., A. Delgado, IDS GeoRadar, 2018). The appearance of strong multiples in the GPR data was not anticipated prior to acquisition.

After cropping the radargram, background correction was performed. The background correction algorithm used in this analysis first computes the mean signal amplitude across each row of a given B-scan. The row-wise means are then subtracted from the B-scan. The expected result of this operation is the reduction of remaining ambient and systematic noise in the form of sub-horizontal bands of enhanced signal amplitude. These high-amplitude bands distort the sought-after information that is directly related to the compact three-dimensional root system.

The third and final step in the GPR pre-processing workflow is near-surface cropping. The shallow subsurface layers create strong reflections in the GPR data unrelated to the root system. Preliminary analysis using the CWT suggested that including the near-surface GPR data overshadowed deeper subsurface features. This was determined by noting that high wavelet fit coefficients appeared in plots that didn’t contain high biomass values, thus biasing the GPR variable towards the plots that exhibited intense surface reflections. Moreover, the cropped region contains a large number of samples collected above to the surface region; this was a potential source of noise. The near-surface zone was removed as

the overwhelming majority of plant biomass was harvested from the area below this zone as is shown in Appendix A, however analysis was simultaneously performed the same B-scans in which this surface region was retained. Results in the analysis section are reported for both methodologies. A representative surface-cropped section is shown in Figure 5.

Fig 4 Region of interest in the analyzed B-scan. Data outside of the red outline was discarded, as it contained primarily noise

Fig 5 Representation of GPR data following surface cropping. Region was chosen by visually determining the 'lowest' point of the first return. Data that was discarded is shown by the shaded region. Data in greyscale was used for further analysis. Data shown here is subset from Figure 5.

2.4 GPR analyses

Following the GPR pre-processing, several analysis methods were used to interpret the processed radargrams. Steps were performed in both the time domain as well as the combined time/frequency domain. The general objective of the analyses is to identify key diagnostic features from the radargrams that correlate to the harvested subsurface biomass.

2.4.1 Time domain signal analysis

In the present study, the behavior of amplitude peaks is used as an indicator of variability within an A-scan signal. The working hypothesis is that one or more of a small panel of candidate amplitude-peak features (see Table 1) are related to mass of belowground material; the use of A-scan features has some precedent in life-science applications of GPR (Barton and Montagu 2004).

Each A-scan was analyzed by either extracting simple summary statistics (such as the mean and standard deviation of the time-varying signal), or by extracting certain information regarding the peak amplitude values. The extracted quantities were then interpreted as candidate features related to the root biomass that was present in the trough at the time of scanning. Specifically, the A-scan features that were extracted included the standard deviation of signal amplitude, the average (mean) signal peak value, the ratio of peak value to the average time interval between peaks, the average amplitude value, the average time interval between peaks, and the number of peaks. This last feature was calculated after the A-scan was truncated as per Figure 3. The foregoing analysis resulted in a set of feature values for each plot. The spatial variability of these features was also explored to understand how each metric varied within an individual plot. While some of the spatial distributions appeared to be normal, others were skewed. Based on this observation, the feature distributions were characterized based on the median as a measure of central tendency, as the median is relatively insensitive to outliers. The median was thus calculated for each plot, and the resulting set of median feature values was correlated with harvested biomass measures.

Table 1 Root density indices key

Index number	Description
1	Standard deviation of A-scan amplitude
2	Mean signal peak amplitude
3	Peak value to peak distance ratio
4	Mean amplitude value
5	Distance between signal amplitude peaks
6	Signal peak count

2.4.2 Time/Frequency Domain Analysis

The continuous wavelet transform (CWT) is a technique that localizes the individual frequency components contained within a time-varying signal. In GPR research, wavelets are often applied, for example to analyze the response of topography (Ouadfeul and Aliouane 2010), to detect landmines (Savelyev and Sato 2004), and to filter signals (Liu et al. 2016). Wavelet application in agricultural root detection is based on the supposition that, similarly to spectrophotometry performed in a wet lab, distinct root sizes or structures will preferentially respond to specific frequency components of a probing electromagnetic wave. While similar to Fourier analysis, wavelet analysis has the key difference of localizing the constituent frequency components of a signal in time, in addition to reporting the relative amplitude of each frequency component. The tabulation of amplitude as a function of scale is performed by convolving scaled and translated versions of a ‘mother’ wavelet function across the extent of a signal trace. The convolution of the signal with the variously scaled and translated 'daughter' wavelets records the relative amplitude of a specific ‘pseudo-frequency’ (hereinafter referred to as a ‘wavelet-pseudo-frequency’, WPS) component at each instant of time within the signal. It is hypothesized that the presence of root mass can be predicted by analyzing the trace-by-trace coherence of WPS components extracted from GPR B-scans of agricultural fields

A novel application of CWT was used herein, similar to the one used in analysis performed by Wernette et. al. (Wernette et al. 2018) based on electromagnetic induction survey data. The observed biomass from the harvest was correlated with sums across each graph of the wavelet coefficients at a given wavelet pseudo-frequency. The mother wavelet chosen for analysis was the complex Morlet wavelet (Morlet et al. 1982a)(Morlet et al. 1982b). The result of the convolution of the complex Morlet wavelet with the GPR trace is a complex signal. We consider only the magnitude of the resulting wavelet coefficients; this is obtained by computing the vector norm of a given transformed trace. These magnitude values are then summed within an agricultural plot to produce a GPR feature that corresponds to a given biomass measurement. A visual representation of this concept is shown in Figure 6. The Morlet wavelet was chosen because it resembles the emitted GPR pulse, with the idea that reflected pulses, though distorted and attenuated by the propagation through the soil medium, would retain the basic frequency content of the emitted pulse.

Fig 6 Annotated plots of continuous wavelet transform for different pseudo-frequencies. Displayed is the information for the WPF 1.12 GHz along with the mass of rhizome portions collected from the trough

3. Results

3.1 Belowground Biomass Analysis

Figure 7 shows the mass distributions of the two types of subsurface structure, fibrous root and rhizome, grouped by depth. It is evident that the variance in the rhizome mass is much higher than that of the fibrous roots. Figure 7 additionally indicates that the subsurface biomass was primarily composed of rhizomes. As rhizomes are more suberized and therefore more persistent in the soil environment than fibrous roots, rhizomes are of great utility in sequestering carbon. If the mass measured in this study is roughly extrapolated (without considering growing conditions, environment, etc.), the amount of deposited belowground material would be ~7300 kg/ha. About 85% of this material would be composed of the comparatively persistent rhizome tissue.

Fig 7 Box and whisker graphs of root and rhizome tissue biomass per depth level. Distributions of both tissue types are shown in 3 sets of 2 graphs, with each box and whisker corresponding to the mass measurement distributions for a given depth level across all 8 agricultural plots for one of the two tissue types

The results of the ANOVA test shown in Table 6 demonstrate that significant differences in belowground biomass variability exist between the depth levels and between belowground tissue types (fibrous roots and rhizomes). A Tukey's HSD post hoc test [25] was conducted to determine whether biomass at different depth levels differed significantly from each other in their mean value. The test additionally determined whether belowground biomass tissue types differed from each other in their mean value. The results of this test (Table 7) show that belowground tissue type differences are highly significant ($p < 0.0001$). Significant differences were also found for between the top and middle ($p < 0.01$), and top and bottom ($p < 0.05$) depth-layers. No significant difference ($p > 0.05$) in mean root-mass was found between the middle and bottom depth layers. These tables can be found in Appendix A. It is evident from Figure 8 b) that the overwhelming majority of rhizome mass is found at levels 2 and 3. A similar trend is followed by the fibrous roots, though to a lesser extent. Also reflected in the graphs is the lower mass values of the first and last plots caused by their smaller sizes.

Fig 8 Line graphs of biomass measurements per depth level for each agricultural plot. Each node represents a single collected sample. **a)** Mass measurements of the fibrous root samples **b)** Mass measurements of rhizomes

Fig 9 Scatterplot of A-scan standard deviation against rhizome biomass. Index 1 was the only measure show to be correlated to the presence of rhizome biomass with an R value of 0.71. This correlation was significant at $p < 0.05$

3.2 Root density indices

All GPR-related features (hereinafter "root indices") listed in Table 1 were tested for correlation with subsampled tissue type, i.e. rhizomatous or fibrous. Of these, only one root index correlated significantly to a belowground biomass tissue type. Index 1 (signal amplitude standard deviation) correlated to rhizome belowground biomass at R=0.71, significance $p< 0.05$. The scatterplot of this index against harvested rhizomatous biomass is shown in Figure 9.

3.3 Time/frequency analysis

The result of the CWT analysis on a given B-scan is a cube wherein each element of the cube's third dimension represents the fit of a daughter wavelet of a given scale to the original signal at that particular location. The concept is illustrated in Figure 10. To obtain the correlation *R*, the real part of the pixel values within each WPF image were first summed, then the sum was normalized by the length of each plot, as shown in Figure 1. The feature investigated here is thus coined as a 'wavelet-pseudo frequency density' (WPFD) measure. This measure was compared to the harvested biomass summed over all depth zones. The biomass measurements were also normalized by the length of their respective plots. The normalization was performed because the sizes of the trough plots varied: the smallest plot was 1.17 m in length, the longest was 3.11 m. The normalization was performed to avoid bias introduced by the different lengths of the harvested plots. Figures 11-14 show the results of the CWT analysis in the form of correlations between fibrous and rhizomatous tissue, respectively, as a function of WPF. Moreover, these figures show the differences in results between the methodology that retained the surface region and the methodology that removed it.

Fig 10 Result of performing continuous wavelet transform on B-scan image. The resulting images demonstrate where and when the mother wavelet convolution resulted in a fit to the original B-scan

Fig 11 Graphs of R values derived from the correlations between plot-harvested **total biomass at combined depth levels** and the WPFD at each WPF. Regions highlighted in red are significant at $p < 0.05$ (No significant correlations for either Rhizome or Total biomass with surface included)

Fig 12 Graphs of R values derived from the correlations between plot-harvested **fibrous root biomass** at each and the WPFD at each WPF. Regions highlighted in red are significant at $p < 0.05$ (No significant correlations for either Rhizome or Total biomass with surface included)

Fig 13 Graphs of R values derived from the correlations between plot-harvested **rhizome biomass** at each and the WPFD at each WPF. Regions highlighted in red are significant at $p < 0.05$ (No significant correlations at middle or lower depths with surface included)

Fig 14 Graphs of R values derived from the correlations **between combined fibrous and rhizome plot-harvested biomass** at each depth at each WPF. Regions highlighted in red are significant at $p < 0.05$ (No significant correlations at lower depth with surface included)

Table 2 Summary of CWT correlation analysis results for Fibrous root biomass. Analysis was performed with the surface included in the data as well as with the surface removed from the data as per Figure 5. Additionally, fibrous mass was evaluated at each of the three depth zones as well as over all of the depth zones combined

Fibrous – Surface Retained				**Fibrous – Surface Removed**			
Depth Range	Peak Frequency (GHz)	R	p	Depth Range	Peak Frequency (GHz)	R	p
0 – 15 cm	41.75	-0.84	0.010	0 – 15 cm	0.64	0.88	0.004
	14.45	-0.87	0.005	15 – 60 cm	1.07	0.84	0.008
	7.38	-0.77	0.024		0.12	0.95	0.000
	0.33	-0.86	0.006		0.08	0.85	0.007
	0.19	-0.77	0.027	60 – 105 cm	0.29	0.90	0.003
15 – 60 cm	0.59	0.77	0.025		0.14	0.75	0.034
60 – 105 cm	N/A	-	-	Combined Depths	0.65	0.85	0.007
Combined Depths	0.17	-0.86	0.006		0.12	0.81	0.016

Table 3 Summary of CWT correlation analysis results for Rhizome biomass. Analysis was performed with the surface included in the data as well as with the surface removed from the data as per Figure 5. Additionally, rhizome mass was evaluated at each of the three depth zones as well as over all of the depth zones combined

Rhizome – Surface Retained				Rhizome – Surface Removed			
Depth Range	Peak Frequency (GHz)	R	p	Depth Range	Peak Frequency (GHz)	R	p
0 – 15 cm	2.85	-0.85	0.008	0 – 15 cm	0.56	0.71	0.047
	0.44	-0.85	0.007	15 – 60 cm	4.89	-0.71	0.048
15 – 60 cm	0.24	0.71	0.049		1.12	0.86	0.006
	-	-	-		0.13	0.86	0.007
	-	-	-		0.08	0.75	0.033
60 – 105 cm	N/A	-	-	60 – 105 cm	0.40	0.75	0.032
Combined Depths	N/A	-	-	Combined Depths	1.05	0.88	0.004

Table 4 Summary of CWT correlation analysis results for total belowground biomass. Analysis was performed with the surface included in the data as well as with the surface removed from the data as per Figure 5. Additionally, total belowground biomass was evaluated at each of the three depth zones as well as over all of the depth zones combined

Fibrous – Surface Retained				Fibrous – Surface Removed			
Depth Range	Peak Frequency (GHz)	R	p	Depth Range	Peak Frequency (GHz)	R	p
0 – 15 cm	42.67	-0.82	0.013	0 – 15 cm	0.57	0.75	0.034
	14.45	-0.90	0.002		-	-	-
	7.54	-0.71	0.047		-	-	-
	0.31	-0.83	0.010		-	-	-
	0.19	-0.82	0.013		-	-	-
	0.14	-0.80	0.018		-	-	-
15 – 60 cm	1.05	0.86	0.006	15 – 60 cm	1.12	0.87	0.005
	0.57	0.77	0.027		0.12	0.88	0.004
	0.12	0.82	0.013		0.08	0.76	0.027
60 – 105 cm	0.86	0.71	0.050	60 – 105 cm	0.40	0.75	0.031
	-	-	-		0.31	0.75	0.033
Combined Depths	N/A	-	-	Combined Depths	1.03	0.87	0.004
	-	-	-		0.13	0.78	0.022

The inclusion or exclusion of the near-surface portion of the radargrams affected the WPF's at which correlations peaked. A summary of all of specific peak information for each root type and depth is given in Table 2, Table 3, and Table 4 for fibrous roots, rhizomes, and total mass respectively. Notably, the inclusion of the near-surface region resulted in strong negative correlations between WPFD and mass density at the 0 – 15 cm depth zone and a smaller number of significantly correlated WPF's at the 15 – 60 cm and 60 – 110 cm depth zones. Conversely, the removal of the near-surface region resulted in more strong positive relationships between WPFD and mass density across all depth zones. This is shown in Figures 11 – 14 as the wider red bands of indicated significance ($p < 0.05$). Little consistency was found between depth zones in terms of significant WPF for each root type. Interestingly, when the near-surface region is removed, all root types correlate significantly to similar WPF ranges. This trend can be seen on the right halves of Figures 11 – 14. Generally, 0 – 15 cm peaked at ~0.6 GHz, 15 – 60 cm peaked at ~1.4 GHz, and 60 – 110 cm peaked at ~0.4 GHz.

4. Discussion

Root detection by GPR shows promise for further development both in theory, since roots present a dielectric contrast to the host soil, and based on previous studies documented in the literature (Barton and Montagu 2004)(Delgado et al. 2017)(Dobreva et al. 2021). The present study assesses the feasibility of root biomass quantification by exploring correlations between features extracted from GPR responses and harvested belowground biomass. A similar A-scan level approach has been previously demonstrated (Barton and Montagu 2004) in which signal features related to tree roots were analyzed. Other studies have adopted an image analysis approach to quantify the presence of belowground biomass. For example, Delgado et. al (Delgado et al. 2017) performed radargram pixel counts to quantify the mass of cassava tubers. Dobreva *et al.* (Dobreva et al. 2021) performed a similar pixel level image analysis to predict peanut yield. While image-analysis approaches should be further investigated for the fibrous root systems of grasses, the lack of a single large, discrete target object characteristic of large roots motivates the current study toward trace-based and time/frequency-based analysis.

Root structures in this study were binary classified as fibrous or rhizomatous, a helpful distinction to explore detectability with ground penetrating radar. The possibility exists of detecting an individual rhizome, although the λ/4 limit (Everett 2013) at 0.9-2.7 GHz prevents resolution of objects less than ~0.88 cm in length. The resolution limit is much larger than a typical diameter of fine roots or root hairs, but potentially of the same scale as rhizomes and the spatial changes in root architecture and/or the root system's zone of influence (i.e. the area within which water interacts with the root system). The relatively large size of the entire root system and its zone of influence is a positive indicator for detectability and belowground mass quantification. However, spatially variable soil moisture affects the interaction between the GPR signal and the root system; an increase in soil water content will reduce the dielectric contrast, and hence reflectivity, of the root and the surrounding soil. Somewhat paradoxically, the reduction in dielectric contrast may assist the detection of smaller roots near the soil surface. The higher dielectric constant of saturated soil slows the signal velocity such that acquired GPR data exhibits higher spatial resolution. This tradeoff is discussed in Liu *et al's* paper (Liu et al. 2018) on GPR detection of wheat roots.

A-scan analysis involves the extraction of features from individual GPR traces. A-scan-level feature extraction methods have previously been used to study the subsurface in non-agricultural settings. Here we describe a few examples. Variation in signal amplitude, for example, was used to characterize a coastal depositional environment (Leandro et al. 2019). Reversal of trace polarity is often indicative of subsurface voids, which aids discovery of buried caskets (Conyers 2015). The first derivative of the signal, instantaneous frequency, and similarity between successive traces are GPR A-scan-level features that were used to characterize sedimentary structures in sand dunes (Zhao et al. 2018). Differences in the two-way-travel time of the 'first return' was used as a feature to understand how soil moisture affects the GPR ground wave (Galagedara et al. 2003). Peaks in A-scan amplitude have been used to extract the classic 'hyperbolae' B-scan level features in GPR (Li and Zhou 2007).

The time-domain analysis of individual signal traces yielded only one GPR feature, or index, with a significant correlation to belowground biomass. As different indices were tested against the two different

root-tissue types, most combinations revealed no significant relationship to the harvested biomass. The total mass and the rhizome mass are very similar, such that these secondary structures of the sorghum hybrid are responsible for a large fraction of the deposited belowground biomass. The dominance of rhizome biomass over fibrous root biomass suggests that time-domain correlations with GPR indices for rhizome biomass and total belowground biomass should be similar. However, while the rhizome biomass correlated significantly to the standard deviation of signal amplitude, the total root biomass did not significantly relate to any of the tested indices. Since rhizomes are an important subsurface structure with high carbon sequestration capacity, the positive correlation result is encouraging, however the insignificant correlation with total belowground biomass contradicts the positive result.

The wavelet analysis produced high correlations at several distinct WPFs, depending on the depth level, tissue type of the biomass under test, and the inclusion or exclusion of the near-surface region of the radargrams. Most interestingly, the correlation switched from strongly negative with surface inclusion to strongly positive with surface exclusion. Moreover, with the surface inclusion analysis, the relationships at the 15 – 60 cm depth zones switched back to being strongly positive. Negative relationships between root biomass and GPR signal features have been reported in previous literature (Liu et al. 2018), and correlations have been shown to switch from negative to positive at progressive depths (Dobreva et al. 2021), however their significance is still not well understood. A possible explanation for negative relationships is that the presence of a root zone may result in less soil compaction and thus cause a weaker reflection at the surface, but this would need to be experimentally confirmed. As the frequency of a GPR signal return corresponding to a large object would typically be low, the expectation is that belowground tissue with a larger radius would be correlated with lower wavelet frequency. In general this was true for the dataset with the surface included, however surface exclusion resulted in a pattern of rhizome tissue showing correlation peaks at higher WPFs than the fibrous root system. This was unexpected, as rhizomes are much larger in diameter than individual roots in the fibrous system. A possible explanation, warranting further study, is that individual fibrous roots do not reflect EM radiation in the frequency range of the current antenna, but are rather detected as an ‘aggregate root zone’. This hypothesis is partially supported by the results shown in Figure 11 as both fibrous roots and rhizomes correlate highly with similar WPF ranges. There is little consistency with which WPFs correlate strongly with biomass as burial depth increases. The lack of a clear relationship between WPF and biomass at each burial depth suggests that morphological structures may respond differently at varying burial depths. The lack of a consistent radar signature could present a significant challenge moving forward, as the eventual goal for this technology is its application in realistic agricultural settings where soil conditions and root mass are not known beforehand. There does appear to be a relationship between the WPF at which high correlations occur and the size of the root structures that are detected. This is shown by the results of the near-surface-exclusion analysis on the right sides of Figure 11, Figure 12, Figure 13, and Figure 14. However, this relationship also requires confirmation, as it is not clearly understood at present. Interestingly, the methodology that correlated belowground biomass to the near-surface-excluded GPR signal without regard to biomass depth performed well on both tissue types (R = 0.81 for fibrous root

tissue, R = 0.88 for rhizome tissue, R = 0.78 for combined biomass). With near-surface-inclusion, this same analysis only produced significant results for the fibrous root system (R = -0.86).

The work described in this paper expands upon methods used in earlier GPR research in the biological sciences. An A-scan-level signal analysis was used to estimate the diameters of coarse roots by observing the time between zero crossings of radar traces in ref. (Barton and Montagu 2004). The use of wavelet transforms in GPR biogeoscience research however is relatively new. Wavelets were discussed in a review by Liu (Liu et al. 2016) who noted their use in various engineering applications primarily as a de-noising and feature extraction technique. The analyses presented herein have adapted wavelets for B-scan feature extraction, thus building on the earlier work. An encouraging feature of these results is that the maximum correlation coefficient at any depth is similar to the results for the shallowest depths, for both the rhizomes and fibrous roots. The close agreement indicates that even though signal attenuation occurred, it was still possible to detect the biomass in the lower depth regions, a result that is highly encouraging for further applications of this technology in a field setting.

The results show that GPR-based proximal sensing belowground biomass of the target sorghum grasses is feasible using both A-scan level analysis and CWT-based time-frequency analysis. This work is an innovative contribution for the following reasons; fine roots were detected to a statistically significant degree, a prototype GPR was applied in an agricultural setting, and the continuous wavelet transform was used to extract signal features. Belowground biomass correlated significantly up to R = 0.92 with GPR features extracted from both types of analysis, thereby demonstrating potential predictive capability. GPR is an emerging proximal sensing technology in agriculture that promises to allow breeders to produce varieties with increased carbon sequestration capabilities; however, extensive field testing and further research is required to achieve this goal. A majority of the PSH12TX09 hybrid's belowground biomass is contained in the rhizome tissue. This finding has positive implications for the use of rhizomatous plants as carbon sequestration targets, as rhizomes are a long-lasting tissue, encourage no-till agricultural practices, and continually deposit organic exudates over their lifetime. Significant relationships exist between radar signal attributes and harvested biomass via time domain analysis and wavelet analysis; however, only one of the proposed root density indices showed excellent performance, and only on a subset of the total root mass. The approach of aggregating A-scans within a given area using basic summary statistics may result in the loss of too much diagnostic information about belowground biomass. Nevertheless, the existing body of work and the correlations found herein between biomass and signal standard deviation indicate that this approach merits continued research regarding root detection. Future research is likely to yield a viable technique for the assessment of belowground carbon storage.

Optimal results from the wavelet analysis are derived from the WPFs that maximally correlate with belowground biomass measures. However, there is a wider range of WPFs at which correlations with belowground biomass are statistically significant. Future work may focus on exploring how the information spanning a wide WPF range which may represent detection of rhizome and roots in unique orientations can be used to predict belowground biomass.

Abbreviations

- Wavelet Pseudo-Frequency (WPF)
- Wavelet Pseudo-Frequency Density (WPFD)
- Ground Penetrating Radar (GPR)
- Continuous Wavelet Transform (CWT)
- Plot – Agricultural plot

Declarations

Acknowledgements

This work was supported with grants from the National Science Foundation award number 1543957—BREAD PHENO: High Throughput Phenotyping Early Stage Root Bulking in Cassava using Ground Penetrating Radar to Dirk B. Hays, and by the Department of Energy of the United States (ARPA-E Award, No. DE-AR0000662)—Development of ground penetrating radar for enhanced root phenotyping and carbon sequestration also to Dirk B. Hays.

References

Allen, M.R., O.P. Dube, W. Solecki, F. Aragón-Durand, W. Cramer, S. Humphreys, M. Kainuma, J. Kala, N. Mahowald, Y. Mulugetta, R. Perez, M. Wairiu and KZ (2018) Global Warming of 1.5°C. An IPCC Special Report on the impacts of global warming of 1.5°C above pre-industrial levels and related global greenhouse gas emission pathways, in the context of strengthening the global response to the threat of climate change,

Barton CVM, Montagu KD (2004) Detection of tree roots and determination of root diameters by ground penetrating radar under optimal conditions. Tree Physiol 24:1323–1331. https://doi.org/10.1093/treephys/24.12.1323

Butnor JR, Doolittle JA, Johnsen KH, et al (2003) Utility of Ground-Penetrating Radar as a Root Biomass Survey Tool in Forest Systems. Soil Sci Soc Am J 67:1607. https://doi.org/10.2136/sssaj2003.1607

Butnor JR, Doolittle JA, Kress L, et al (2001) Use of ground-penetrating radar to study tree roots in the southeastern United States. Tree Physiol 21:1269–1278. https://doi.org/11696414

Cassidy N (2009) Ground penetrating radar data processing, modelling and analysis, First Edit. Elsevier

Conyers LB (2015) Analysis and interpretation of GPR datasets for integrated archaeological mapping. Near Surf Geophys 13:645–651. https://doi.org/10.3997/1873-0604.2015018

Crop Phenomics L GPR Studio

Delgado A, Hays DB, Bruton RK, et al (2017) Ground penetrating radar: A case study for estimating root bulking rate in cassava (Manihot esculenta Crantz). Plant Methods 13:. https://doi.org/10.1186/s13007-017-0216-0

Dobreva ID, Ruiz-Guzman HA, Barrios-Perez I, et al (2021) Thresholding Analysis and Feature Extraction from 3D Ground Penetrating Radar Data for Noninvasive Assessment of Peanut Yield. Remote Sens 13:1896. https://doi.org/10.3390/rs13101896

Everett M (2013) Near-surface Applied Geophysics

Galagedara LW, Parkin GW, Redman JD (2003) An analysis of the ground-penetrating radar direct ground wave method for soil water content measurement. Hydrol Process 17:3615–3628. https://doi.org/10.1002/hyp.1351

García-robledo C, Kuprewicz EK, Staines CL, et al (2016) Limited tolerance by insects to high temperatures across tropical elevational gradients and the implications of global warming for extinction. 113:. https://doi.org/10.1073/pnas.1507681113

Gebhart DL, Johnson HB, Mayeux HS, Polleym HW (1994) The CRP increases oil organic carbon. J soil water Conserv 49:488–492

Jessup RW, Klein RR, Burson BL, et al (2017) Registration of Perennial Sorghum bicolor × S. propinquum Line PSH12TX09 . J Plant Regist 11:76–79. https://doi.org/10.3198/jpr2015.09.0054crgs

Kerry JT, Álvarez-noriega M, Álvarez-romero JG, et al (2017) Global warming and recurrent mass bleaching of corals. https://doi.org/10.1038/nature21707

Kim K, Scott WR (2005) Design of resistively loaded vee dipole for ultrawide-band ground-penetrating radar applications. IEEE Trans Antennas Propag 53:2525–2532. https://doi.org/10.1109/TAP.2005.852292

Lane HM, Murray SC (2021) High Throughput can produce better decisions than high accuracy when phenotyping plant populations. Crop Sci. https://doi.org/10.1002/csc2.20514

Leandro CG, Barboza EG, Caron F, de Jesus FAN (2019) GPR trace analysis for coastal depositional environments of southern Brazil. J Appl Geophys 162:1–12. https://doi.org/10.1016/j.jappgeo.2019.01.002

Ledo A, Smith P, Zerihun A, et al (2020) Changes in soil organic carbon under perennial crops. Glob Chang Biol 26:4158–4168. https://doi.org/10.1111/gcb.15120

Lemus R, Lal R (2005) Bioenergy crops and carbon sequestration. CRC Crit Rev Plant Sci 24:1–21. https://doi.org/10.1080/07352680590910393

Li TJ, Zhou ZO (2007) Fast extraction of hyperbolic signatures in GPR. 2007 Int Conf Microw Millim Wave Technol ICMMT '07 3–5. https://doi.org/10.1109/ICMMT.2007.381489

Liu X, Dong X, Leskovar DI, et al (2018) Ground penetrating radar (GPR) detects fine roots of agricultural crops in the field. Plant Soil 517–531

Liu X, Dong X, Leskovar DI (2016) Ground penetrating radar for underground sensing in agriculture: A review. Int Agrophysics 30:533–543. https://doi.org/10.1515/intag-2016-0010

Montoya TP, Smith GS (1996) Resistivity-loaded Vee antennas for short-pulse ground penetrating radar. IEEE Antennas Propag Soc AP-S Int Symp 3:2068–2071. https://doi.org/10.1109/aps.1996.550015

Morlet J, Arens G, Fourgeau E, Giard D (1982a) Wave propagation and sampling theory - Part I. Complex signal and scattering in multilayered media. Geophysics 47:203–221. https://doi.org/10.1190/1.1441328

Morlet J, Arens G, Fourgeau E, Giard D (1982b) Wave propagation and sampling theory - Part II. Sampling theory and complex waves. Geophysics 47:222–236. https://doi.org/10.1190/1.1441329

Nuzzo L, Alli G, Guidi R, et al (2014) A new densely-sampled Ground Penetrating Radar array for landmine detection. In: Proceedings of the 15th International Conference on Ground Penetrating Radar. IEEE, pp 969–974

Ouadfeul SA, Aliouane L (2010) Multiscale analysis of 3D GPR data using thecontinuous Wavelet Transform. Proc 13th Internarional Conf Gr Penetrating Radar, GPR 2010 1–4. https://doi.org/10.1109/ICGPR.2010.5550177

Paez-Garcia A, Motes CM, Scheible WR, et al (2015) Root traits and phenotyping strategies for plant improvement. Plants 4:334–355. https://doi.org/10.3390/plants4020334

Resource N, Collins F (2001) GRASSLAND MANAGEMENT AND CONVERSION INTO GRASSLAND : EFFECTS ON SOIL CARBON. 11:343–355

Savelyev TG, Sato M (2004) Comparative analysis of UWB deconvolution and feature-extraction algorithms for GPR landmine detection. Detect Remediat Technol Mines Minelike Targets IX 5415:1008. https://doi.org/10.1117/12.541748

Schmidt GA, Ruedy RA, Miller RL, Lacis AA (2010) Attribution of the present-day total greenhouse effect. J Geophys Res Atmos 115:1–6. https://doi.org/10.1029/2010JD014287

Shen X, Foster T, Baldi H, et al (2019) Quantification of soil organic carbon in biochar-amended soil using ground penetrating radar (GPR). Remote Sens 11:1–12. https://doi.org/10.3390/rs11232874

Thomas H, Thomas HM, Ougham H (2000) Annuality, perenniality and cell death. J Exp Bot 51:1781–1788. https://doi.org/10.1093/jexbot/51.352.1781

Utsi E (2017) Ground Penetrating Radar: theory and practice

Wernette P, Houser C, Weymer BA, et al (2018) Influence of a spatially complex framework geology on barrier island geomorphology. Mar Geol 398:151–162. https://doi.org/10.1016/j.margeo.2018.01.011

Xiong S, Thomas K (2010) Carbon-allocation dynamics in reed canary grass as affected by soil type and fertilization rates in northern Sweden. Acta Agric Scand Sect B Soil Plant Sci 60:24–32. https://doi.org/10.1080/09064710802558518

Zhao W, Forte E, Fontolan G, Pipan M (2018) Advanced GPR imaging of sedimentary features: Integrated attribute analysis applied to sand dunes. Geophys J Int 213:147–156. https://doi.org/10.1093/gji/ggx541

(2016) Attribution of extreme weather events in the context of climate change. National Academies Press

Figures

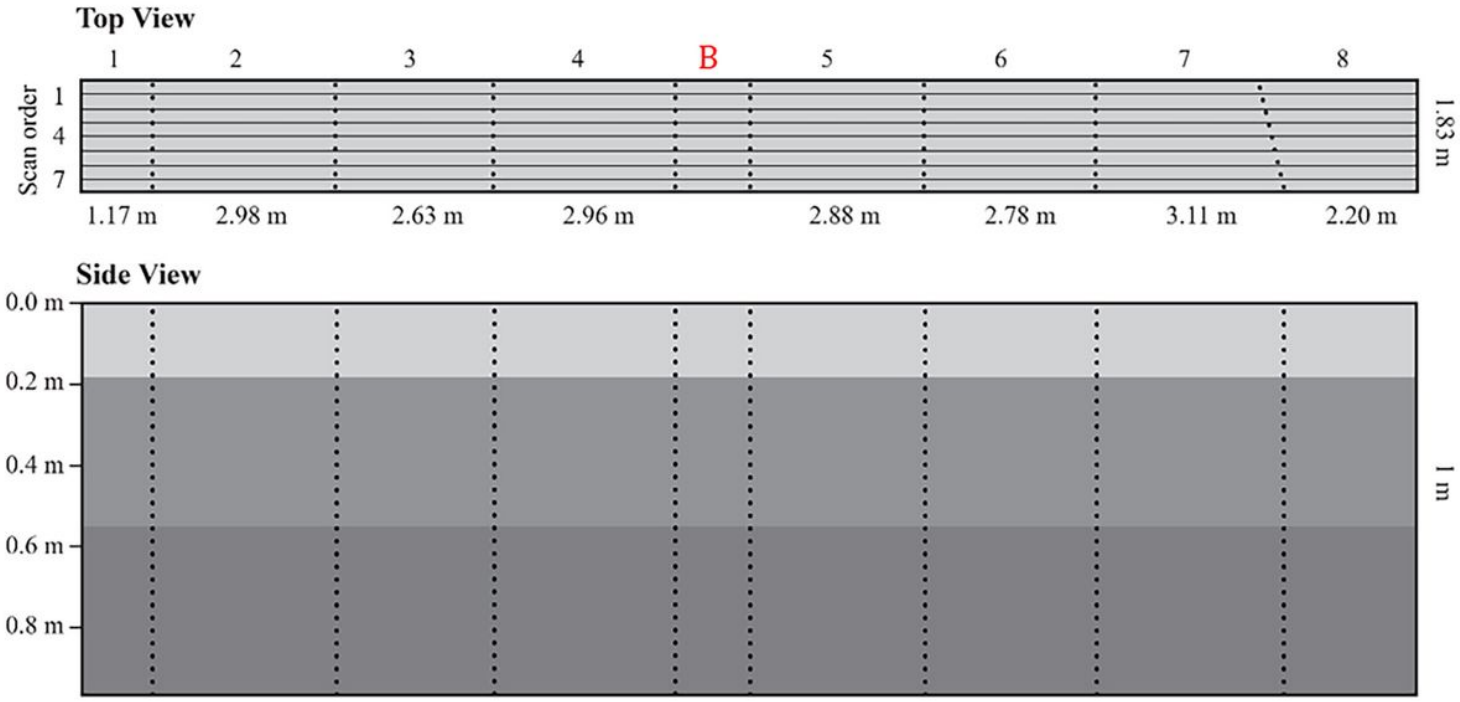

Figure 1

Plots and depth levels in the trough environment. From left to right, plots are numbered 1 – 8 (see top view). The space labeled ‘B’ was designated as a blank area and no associated mass was harvested. The different depth zones are demarcated with different shades of gray

Figure 2

Image of artificial trough environment. (left) Belowground biomass following trough washing process. Pictured are the three depth layers separated by the green nylon netting. (right). Artificial trough environment during growing season

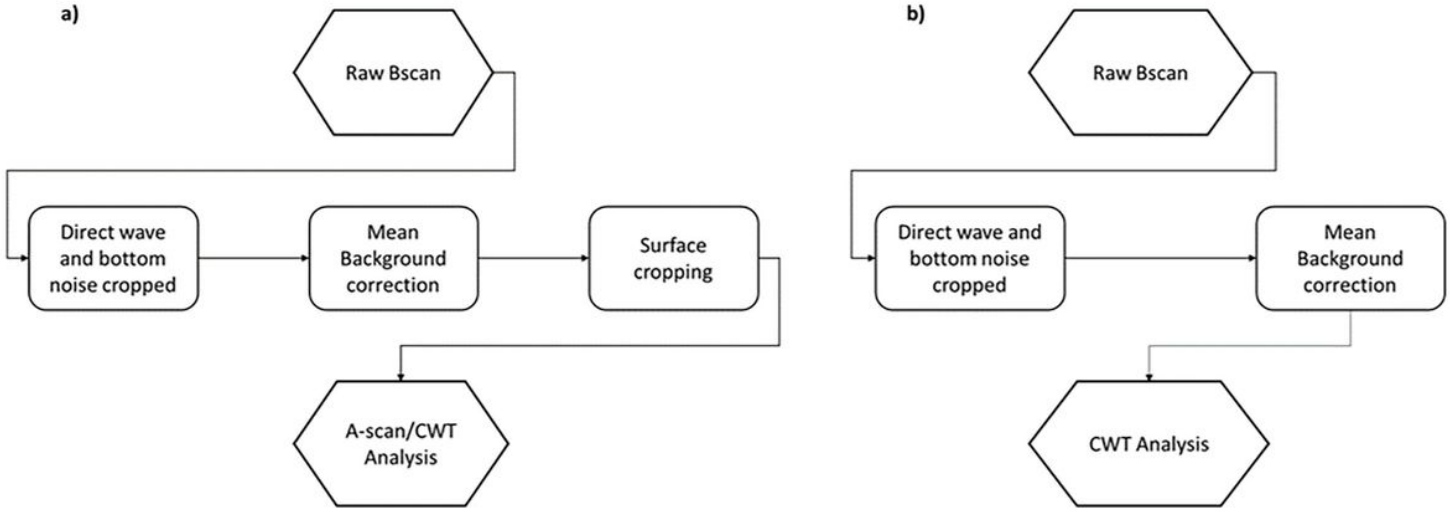

Figure 3

Processing flowcharts. Chart a) shows the processing steps used to prepare GPR data for the A-scan analysis and half of the CWT analysis. Chart b) shows the processing steps used to prepare GPR data for the second half of the CWT analysis

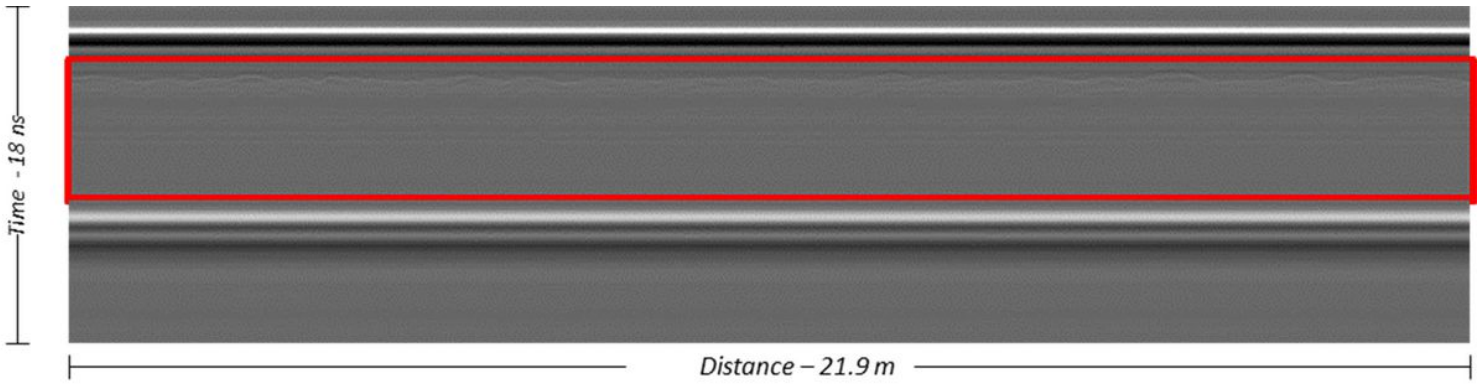

Figure 4

Region of interest in the analyzed B-scan. Data outside of the red outline was discarded, as it contained primarily noise

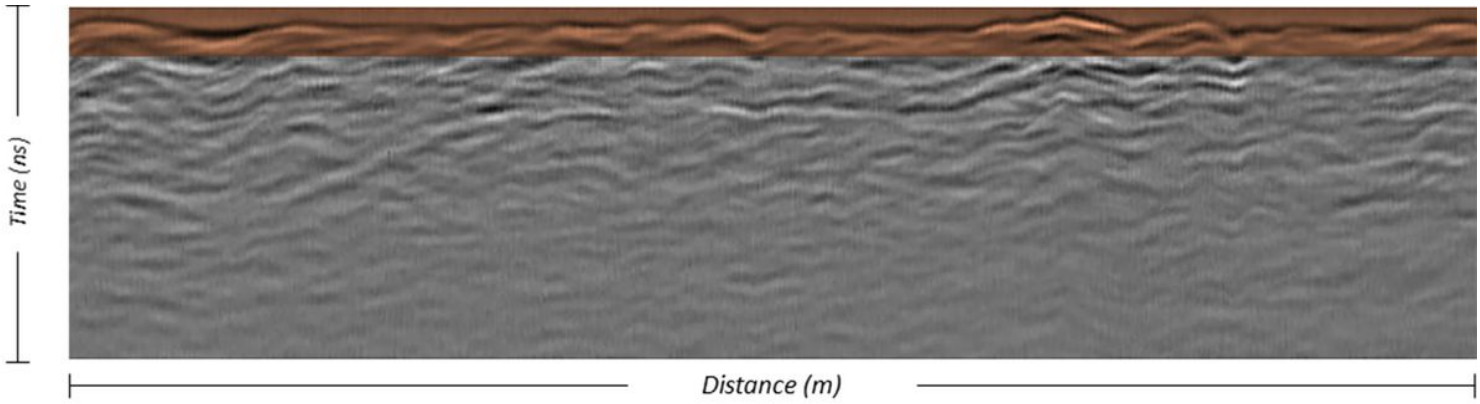

Figure 5

Representation of GPR data following surface cropping. Region was chosen by visually determining the 'lowest' point of the first return. Data that was discarded is shown by the shaded region. Data in greyscale was used for further analysis. Data shown here is subset from Figure 5.

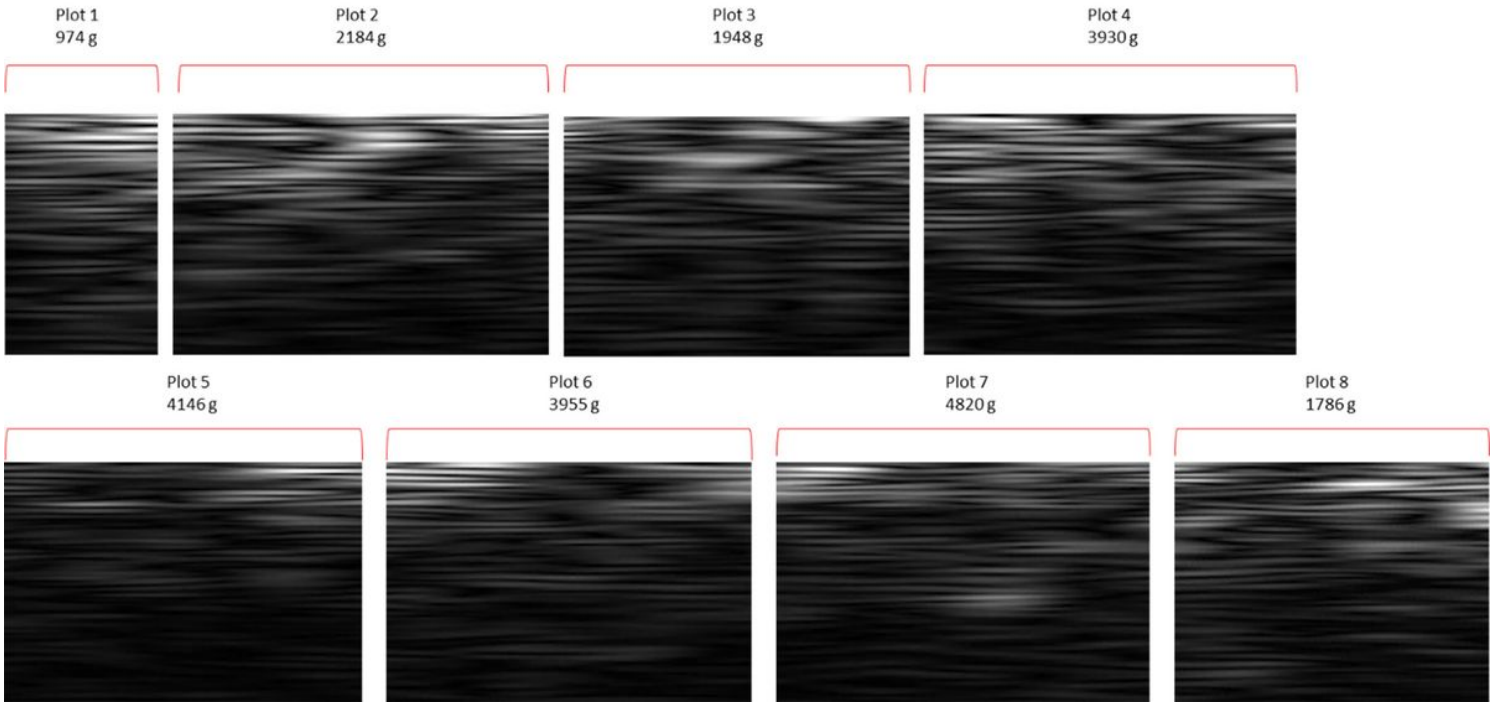

Figure 6

Annotated plots of continuous wavelet transform for different pseudo-frequencies. Displayed is the information for the WPF 1.12 GHz along with the mass of rhizome portions collected from the trough

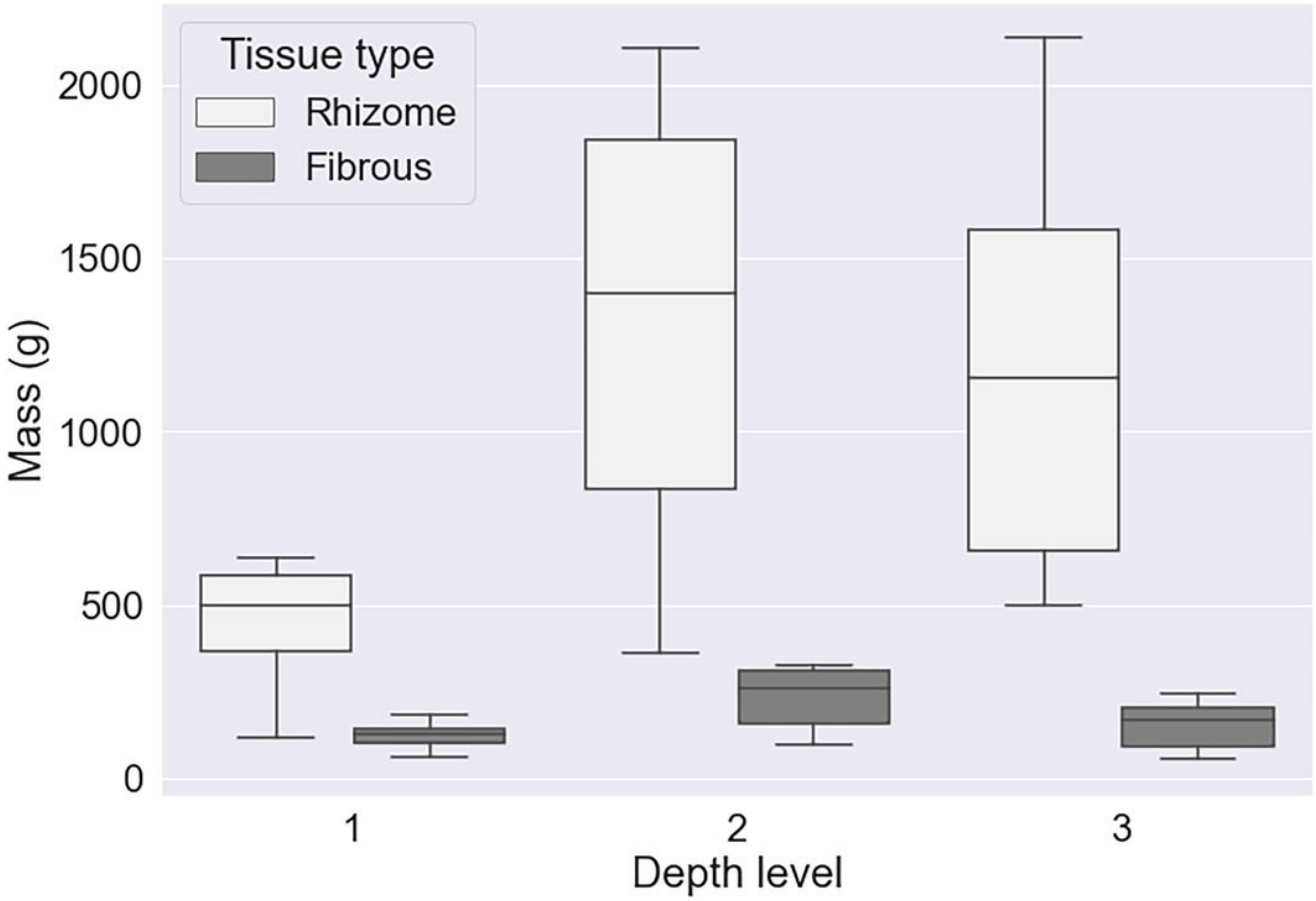

Figure 7

Box and whisker graphs of root and rhizome tissue biomass per depth level. Distributions of both tissue types are shown in 3 sets of 2 graphs, with each box and whisker corresponding to the mass measurement distributions for a given depth level across all 8 agricultural plots for one of the two tissue types

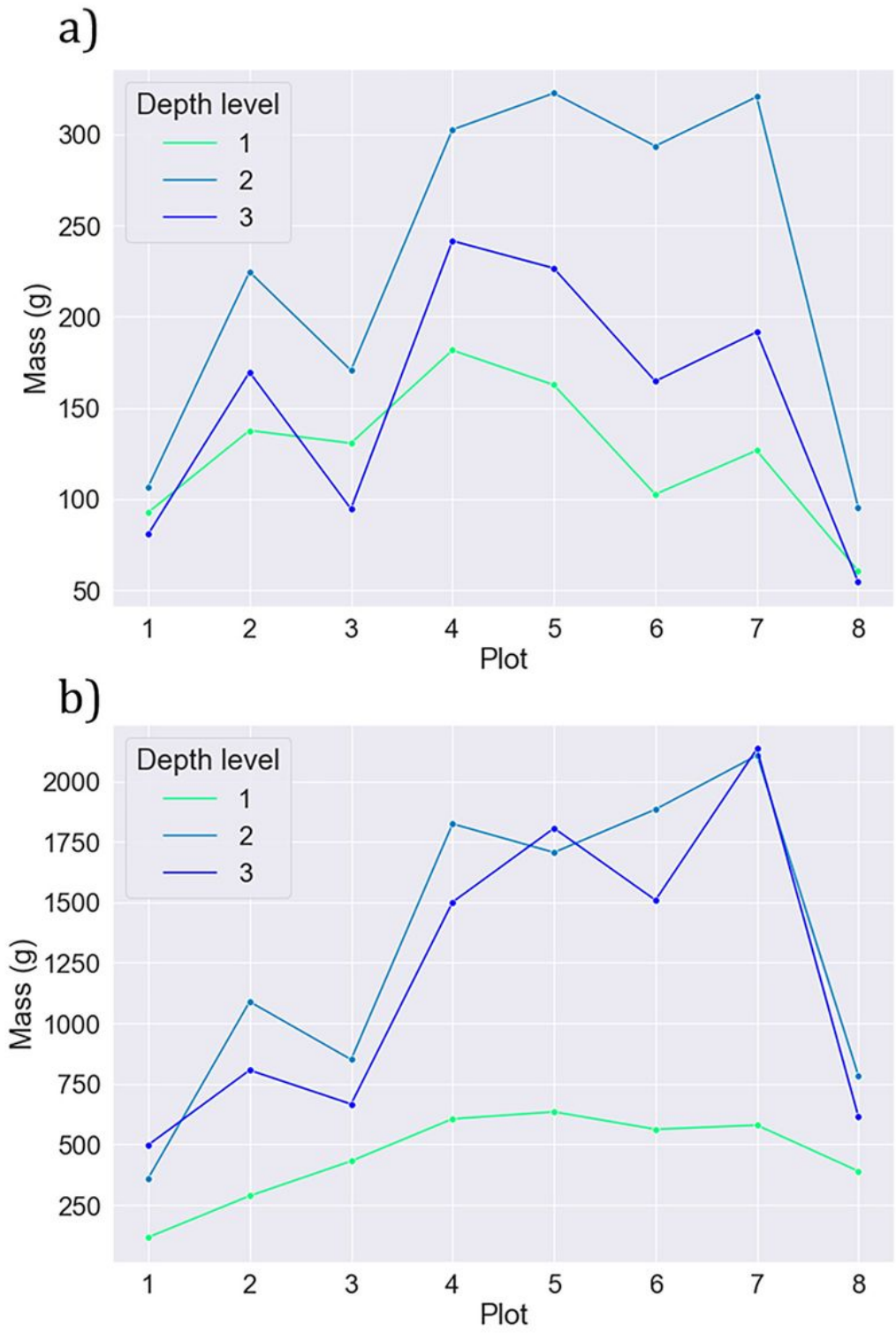

Figure 8

Line graphs of biomass measurements per depth level for each agricultural plot. Each node represents a single collected sample. a) Mass measurements of the fibrous root samples b) Mass measurements of rhizomes

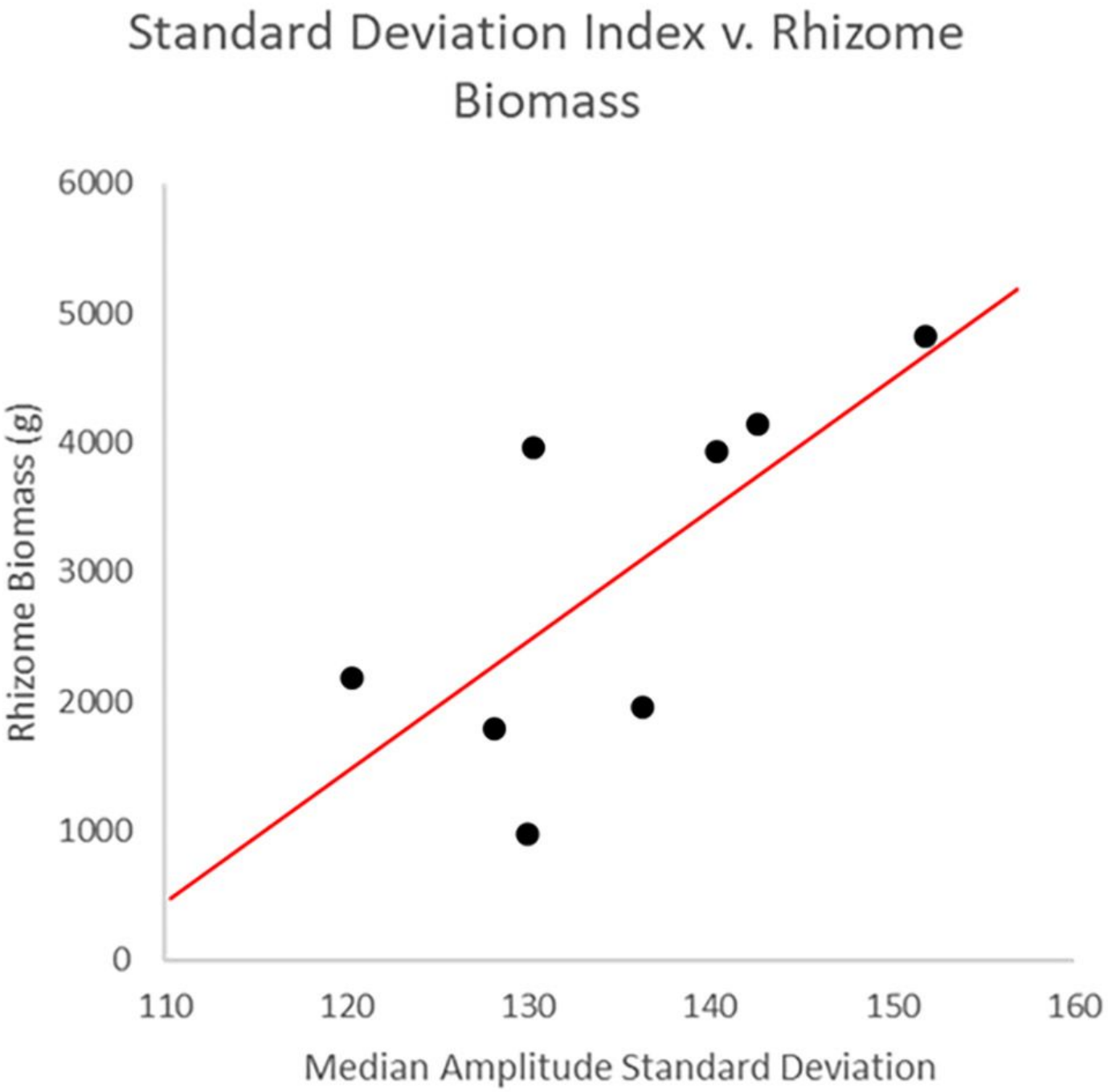

Figure 9

Scatterplot of A-scan standard deviation against rhizome biomass. Index 1 was the only measure show to be correlated to the presence of rhizome biomass with an R value of 0.71. This correlation was significant at $p < 0.05$

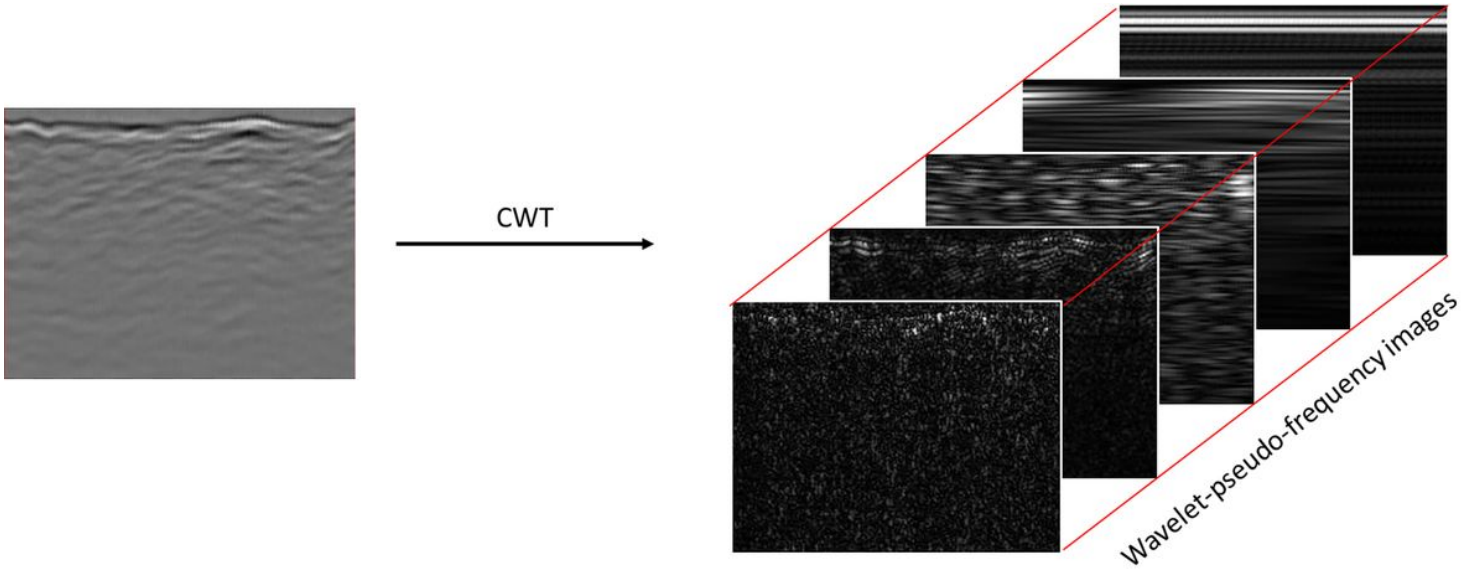

Figure 10

Result of performing continuous wavelet transform on B-scan image. The resulting images demonstrate where and when the mother wavelet convolution resulted in a fit to the original B-scan

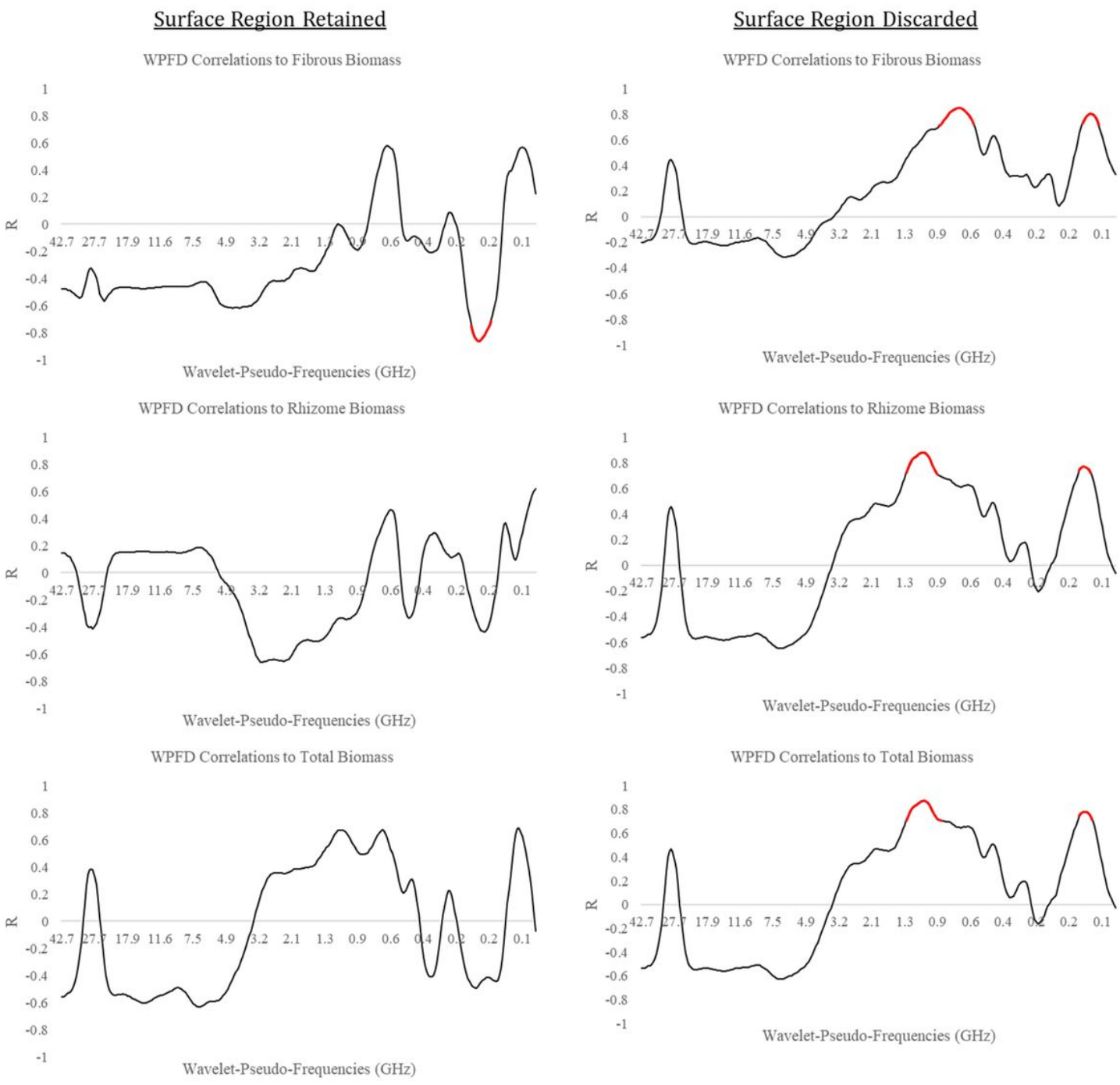

Figure 11

Graphs of R values derived from the correlations between plot-harvested total biomass at combined depth levels and the WPFD at each WPF. Regions highlighted in red are significant at $p < 0.05$ (No significant correlations for either Rhizome or Total biomass with surface included)

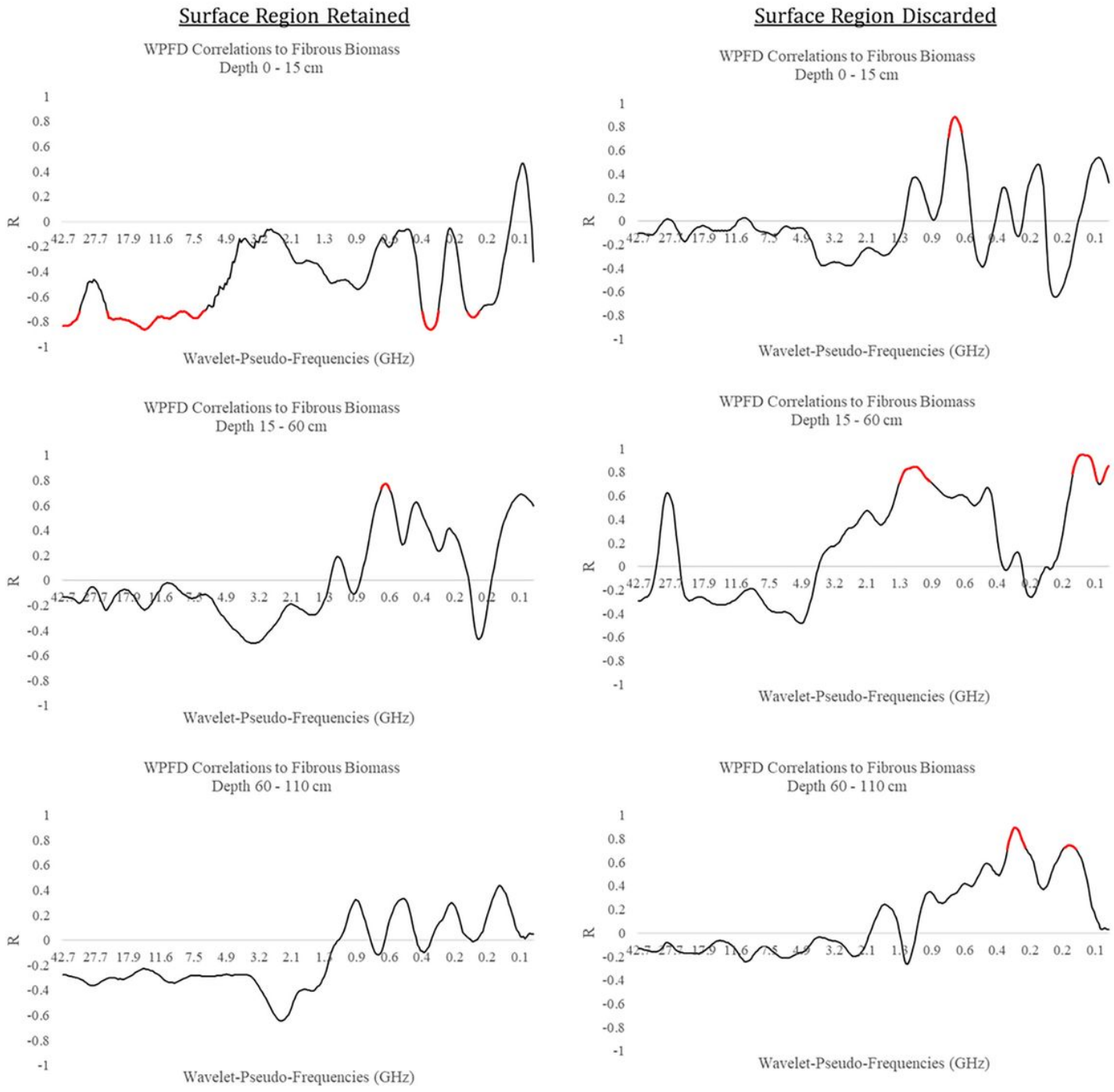

Figure 12

Graphs of R values derived from the correlations between plot-harvested fibrous root biomass at each and the WPFD at each WPF. Regions highlighted in red are significant at $p < 0.05$ (No significant correlations for either Rhizome or Total biomass with surface included)

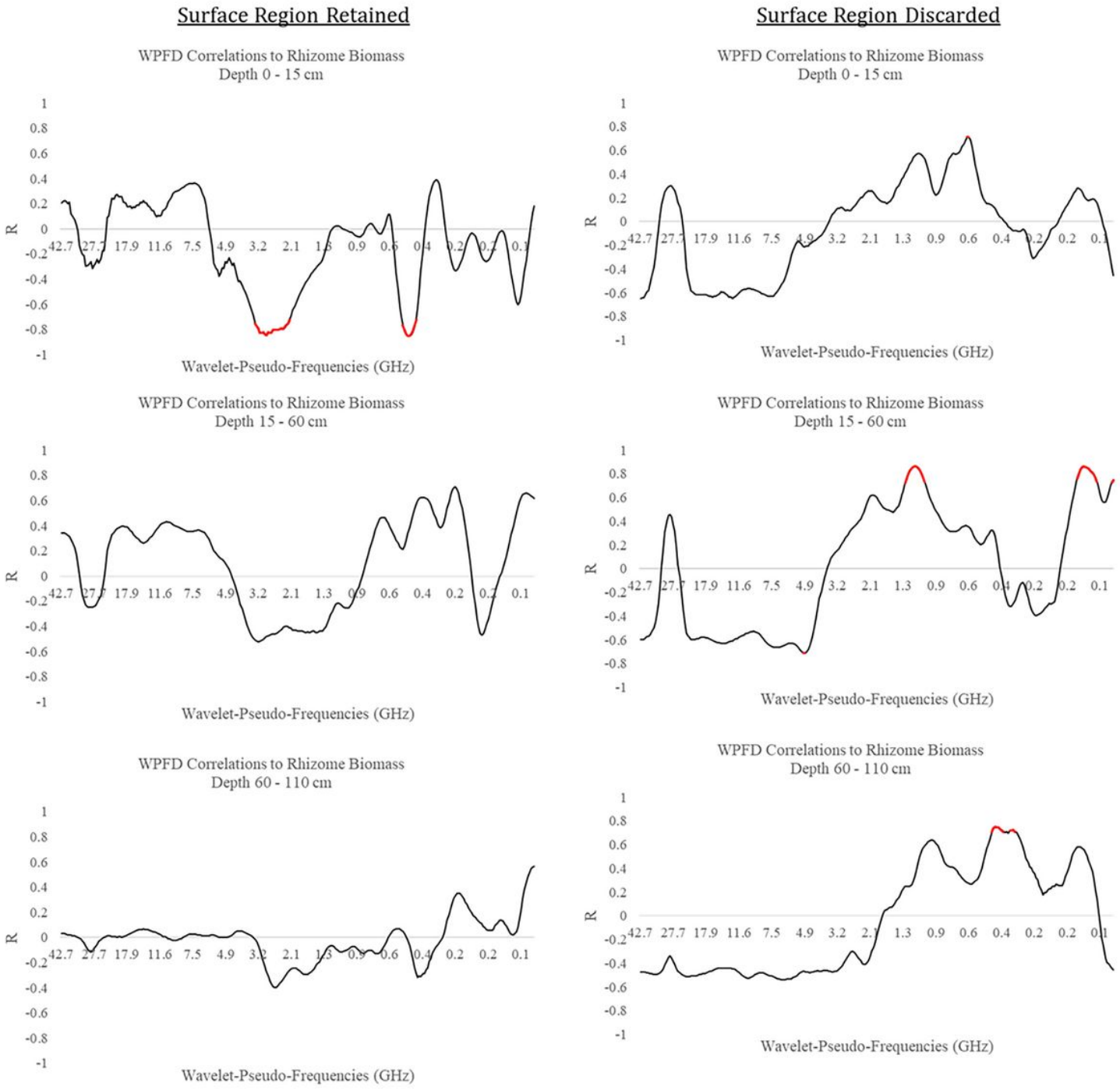

Figure 13

Graphs of R values derived from the correlations between plot-harvested rhizome biomass at each and the WPFD at each WPF. Regions highlighted in red are significant at $p < 0.05$ (No significant correlations at middle or lower depths with surface included)

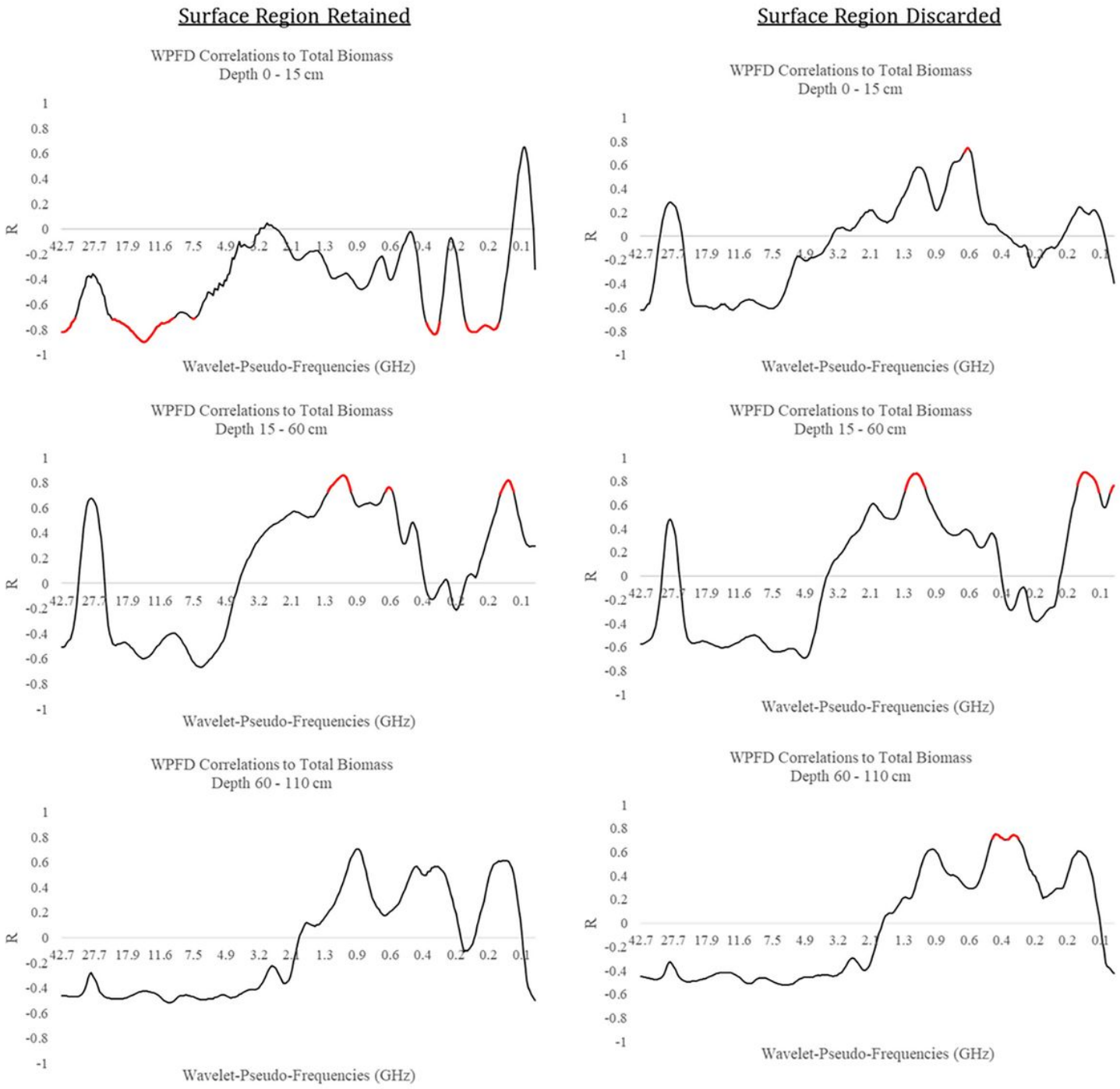

Figure 14

Graphs of R values derived from the correlations between combined fibrous and rhizome plot-harvested biomass at each depth at each WPF. Regions highlighted in red are significant at $p < 0.05$ (No significant correlations at lower depth with surface included)

Supplementary Files

This is a list of supplementary files associated with this preprint. Click to download.

- AppendixA.docx